JOURNAL OF GEOPHYSICAL RESEARCH, VOL. 105, NO. D4, PAGES 4949–4959, FEBRUARY 27, 2000

Determination of an effective spectral surface albedo from ground–based global and direct UV irradiance measurements

A. Kylling,[1,2] T. Persen,[3,4] B. Mayer,[5] and T. Svenøe[6,7]

Abstract. Ultraviolet radiation may be enhanced by the presence of snow cover. For areas with snow the surface is often highly inhomogeneous owing to the presence of low–albedo surfaces together with snow–covered surfaces. In order to better understand the coupling between snow cover, surface albedo, and UV radiation, an estimate of an effective albedo for such highly inhomogeneous surfaces is required. In this paper a method to derive an effective wavelength dependent Lambertian surface albedo in the UV and visible part of the spectrum is described. The retrieval method is used to analyze direct and global irradiance measurements performed in the wavelength region 320–500 nm during the winter–spring–summer seasons of 1997 in Tromsø, Norway. The derived albedo reached a maximum of 0.57 and 0.78 at 320 and 450 nm, respectively, when the snow depth was at maximum. The corresponding values for completely snow–free conditions were 0.08 and 0.16. The absolute uncertainty in these values is estimated to be 0.1 at the shortest wavelengths and 0.2 at the higher wavelengths. Calculations with a three–dimensional Monte Carlo model indicate that the open waters surrounding Tromsø all the year round decrease the effective albedo by approximately 0.2 compared to a completely snow–covered surface.

1. Introduction

Surfaces with a high albedo enhance the amount of UV radiation reaching the Earth's surface [*Lenoble*, 1998]. The albedo of a number of surface types has been measured in the UV both at high spectral resolution [*Feister and Grewe*, 1995; *McKenzie et al.*, 1996] and by filter instruments [*Blumthaler and Ambach*, 1988]. However, such measurements of local albedo values are not sufficient for the interpretation of radiation measurements if the surroundings of the measurement site are highly inhomogeneous because the downwelling irradiance is affected by a more or less large area around the measurement site. An example is the observation site at the Auroral Observatory, Tromsø, Norway. It is located on top of the island of Tromsø (65 m above sea level (asl), 69.65° N, 18.95° E). Tromsø is surrounded by open water all the year round, but the mountainous areas to the west, east, north, and south are snow covered during large parts of the year (Figure 1). In addition to the surrounding ocean and mountains, nearby trees, buildings, and roads add to the difficulties of estimating an effective surface albedo.

Using measurements of downwelling global and diffuse irradiance, *King and Herman* [1979] and *King* [1979] retrieved an effective surface albedo and an aerosol refractive index at two wavelengths under the assumption that neither varies throughout the day. *Ricchiazzi et al.* [1995] retrieved simultaneously a cloud–scattering optical depth and local surface albedo for Palmer Station, Antarctica. They utilized global irradiance data from a ground–based multichannel radiometer in conjunction with radiative transfer modeling. Both the surface albedo and the cloud optical thickness were assumed to be constant with wavelength. *Ricchiazzi and Gautier* [1998, p. 6161] further investigated the effect of surface heterogeneity and topography on the radiation environment of Palmer Station using Monte Carlo techniques. They found that "the effective albedo ... is affected by regions surprisingly far from the point of interest." *Degünther et al.* [1998] investigated the same effect in more general terms with similar conclusions.

Here we describe a new method to derive an effective spectral surface albedo and use it to analyze data

[1]Norwegian Institute for Air Research, Kjeller.

[2]Also at Department of Geophysics, University of Oslo, Oslo.

[3]Auroral Observatory, University of Tromsø, Tromsø, Norway.

[4]Now at Kværner Engineering, Stavanger, Norway.

[5]National Center for Atmospheric Research, Boulder, Colorado.

[6]Norwegian Institute for Air Research, Tromsø.

[7]Also at Auroral Observatory, University of Tromsø, Tromsø, Norway.

Paper number 1999JD900304
0148-0227/00/1999JD900304$09.00

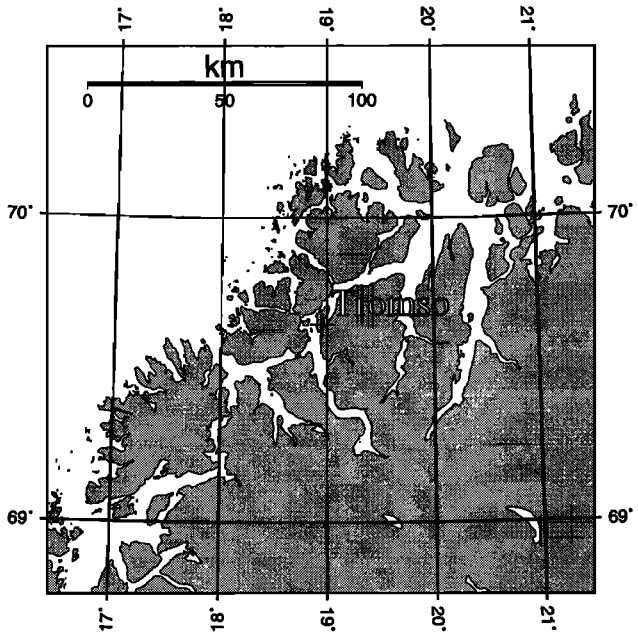

Figure 1. Map of Tromsø (center of map) and surrounding areas. Shaded areas indicate land, and open areas indicate water. The measurement site is located in the center of the map (cross) on the island of Tromsø.

recorded in 1997 in Tromsø, Norway. *King and Herman* [1979] assumed that the albedo and the aerosol refractive index stayed constant during the day. In contrast, the present method assumes realistic values for the aerosol single–scattering albedo and phase function but allows the albedo to vary throughout the day. Furthermore, the use of spectral direct and global measurements covering the whole of the UV and part of the visible regions of the spectrum allows a wavelength dependent albedo to be deduced.

The paper is organized as follows. First, the method used to estimate the albedo is described. A description of the instrumentation and the radiative transfer model follows together with a sensitivity analysis of the albedo estimation method. Next, the albedo results are presented, and the effect of the surrounding ocean is discussed. Finally, the results are summarized.

2. Method

The surface albedo Λ is defined as the ratio between the upwelling, $E^{\uparrow}$, and downwelling, $E^{\downarrow}$, irradiances at the surface:

$$\Lambda = \frac{E^{\uparrow}}{E^{\downarrow}}. \tag{1}$$

All quantities in (1) depend on wavelength. It is omitted in (1)–(6) for simplicity.

A nonzero surface albedo will increase the global (direct plus diffuse) downwelling irradiance at the surface. The magnitude of this increase may be estimated by starting with the downwelling global irradiance if there were no albedo, $E_{\text{global}}(\Lambda = 0)$. For a nonzero albedo a fraction Λ of $E_{\text{global}}(\Lambda = 0)$ is reflected upward by the surface. Here Lambertian reflection is assumed; that is, the reflected radiation is isotropic. Because of scattering in the atmosphere, a fraction, $\overline{s}$, of the upwelling irradiance is scattered back to the surface giving an increase of the global irradiance by a factor $(1+\overline{s}\Lambda)$. Part of this is again reflected and scattered back, and so on, to give the global irradiance for $\Lambda > 0$ as

$$\begin{aligned} E_{\text{global}}(\Lambda) &= E_{\text{global}}(0)\sum_{i=0}^{\infty}(\overline{s}\Lambda)^i \\ &= E_{\text{global}}(0)\cdot\frac{1}{1-\overline{s}\Lambda}. \end{aligned} \tag{2}$$

We note that (2) is a geometric series. An alternative derivation of (2) is provided by *Lenoble* [1998]. It should also be mentioned that $\overline{s}\Lambda$ does not depend on solar zenith angle, implying that the enhancement of global irradiance due to reflection at the Earth's surface is independent of solar zenith angle, given that the surface is a Lambertian reflector. Equation (2) may be solved for the surface albedo Λ provided that all other quantities are known with sufficient accuracy. However, in the UV region of the spectrum, relatively large uncertainties are associated with the absolute values of the irradiance. For instruments where the absolute calibration errors of the direct and global irradiances are affected equally, it is preferable to use the ratio, R, between the direct irradiance and the global irradiance:

$$R = \frac{E_{\text{direct}}}{E_{\text{global}}} = \frac{T_{\text{direct}}}{T_{\text{global}}(0)\cdot\frac{1}{1-\overline{s}\Lambda}}. \tag{3}$$

Here $T_{\text{direct}} = E_{\text{direct}}/E_{\odot}$ is the direct transmittance, and $T_{\text{global}}(0) = E_{\text{global}}(0)/E_{\odot}$ is the global transmittance for a surface albedo of zero, where $E_{\odot}$ is the extraterrestrial solar flux. Given sufficent and accurate information about the state of the atmosphere, the quantities T_{direct} and $T_{\text{global}}(0)$ are readily calculated by a radiative transfer model. The reflectivity of the atmosphere, $\overline{s}$, may also be calculated using a radiative transfer model by evaluating (2) for $\Lambda = 0$ and $\Lambda = 1$:

$$\overline{s} = 1 - \frac{T_{\text{global}}(0)}{T_{\text{global}}(1)}. \tag{4}$$

With knowledge of the ratio, R, of the measured direct and global irradiance the albedo can then be calculated by solving (3) for Λ:

$$\Lambda = \frac{1}{\overline{s}}\left(1 - \frac{R\cdot T_{\text{global}}(0)}{T_{\text{direct}}}\right). \tag{5}$$

An alternative derivation of (5) is given in the appendix.

Figure 2 shows model calculations of the ratio R as a function of wavelength, for two solar zenith angles and albedos between 0.0 and 1.0. The relative change in reflectivity R with albedo Λ can be calculated from (3):

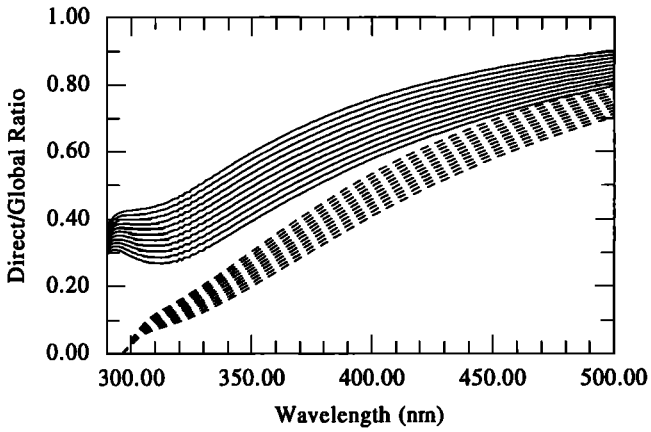

Figure 2. Model–calculated direct to global irradiance ratios R as a function of wavelength. Ratios for two solar zenith angles, 45° (solid lines) and 70° (dashed lines), are shown. For each solar zenith angle the ratio is shown for albedos varying from 1.0 (lower solid and dashed lines) to 0.0 (upper solid and dashed lines) 0.0 in steps of 0.1.

$$\frac{1}{R}\frac{\partial R}{\partial \Lambda} = -\frac{1}{1/\bar{s} - \Lambda}. \tag{6}$$

The relative change of reflectivity is independent of solar zenith angle, and its absolute value increases with increasing $\bar{s}$ and Λ. The method therefore is most sensitive at high $\bar{s}$. As will be shown in section 7, $\bar{s}$ has its maximum around 320 nm and is decreasing toward shorter and longer wavelengths. The method therefore works best in the UV–B and lower UV–A parts of the spectrum, and the uncertainty increases toward visible wavelengths, as is also obvious from Figure 2. The sensitivity of the method with respect to experimental uncertainties and model assumptions will be discussed in section 5. As the method is based on the accurate simulation of R, we restrict its application to cloudless sky.

3. Instrumentation and Measurements

During the 1997 season a spectroradiometer located in Tromsø, Norway, regularly measured the direct and global irradiances. The spectroradiometer was a Jobin–Yvon HR 320 single monochromator with diffraction gratings (1200 lines per millimeter) operating in the first order. The full width at half maximum (FWHM) of the slit function is 0.68 nm. The entrance optics consist of a flat teflon diffuser used for global irradiance measurements and a small telescope for direct irradiance measurements. The telescope is made of a small lens and baffling. It is dimensioned to give a field of view of 1.8°. A split optical fibre bundle guides either the direct or the global irradiance to the monochromator. Electronically controlled shutters at the tips of the split optical fibre bundle allow the direct and the global irradiance to be measured near simultaneously for a single wavelength. A global and direct scan covers the wavelength range from 290 to 600 nm with steps of 1.0 nm. Since the spectroradiometer is a single monochromator, only results for wavelengths longward of 320 nm will be presented here. Furthermore, since the albedo estimation method is not sensitive enough for longer wavelengths, results longward of 500 nm will not be presented here. A simultaneous direct and global scan takes about 12 min. In normal operation a direct and global scan was made every 20 min. The spectroradiometer is calibrated against a 1000 W quartz–halogen standard lamp traceable to the National Institute of Standards and Technology (NIST). The direct beam was calibrated by measuring the relative transmission between the direct and global entrance optics. This was done by measuring the 1000 W lamp with global input optics at the prescribed NIST distance of 50 cm. The direct channel next measured the same lamp at a distance of 400 cm to allow the telescope to view the whole filament of the lamp. The results were transferred to 50 cm using the inverse square law as recommended by NIST. The absolute calibration of the direct channel was then established through the relative ratio between two channels and the absolute calibration of the global irradiance. The error in the relative transmission between the direct and global entrance optics is estimated to be less than 5%. Hence the calibration–related error in the ratio R derived from the measured direct and global irradiance, equation (3), is less than 5%. Another source of uncertainty is the deviation of the angular response of the entrance optics from the ideal cosine. The angular response of the diffuser has been determined in the laboratory and used to correct the global irradiance measurements. Assuming an isotropic distribution of the sky radiance, the magnitude of the correction for the results reported here ranges between 9 and 15%. The overall uncertainty in the cosine correction procedure is estimated to be 4–5%.

The measurements of the direct irradiance allow the total ozone column and the aerosol optical depth to be determined. A method similar to the one described by *Mayer et al.* [1997] was used. However, while Mayer et al. used the ATLAS 2 extraterrestrial spectrum [*Woods et al.*, 1996], we used an extraterrestrial spectrum constructed from two sources: Below 312 nm the ATLAS 3 spectrum shifted to air wavelengths was used (M. E. VanHoosier, personal communication, 1996), and above 312 nm we used an extraterrestrial spectrum measured by the spectroradiometer using the Langley plot method. To check the quality of the spectrum above 312 nm we compared it with the ATLAS 3 spectrum for wavelengths between 312 and 407.8 nm, with the ATLAS 2 spectrum [*Woods et al.*, 1996] between 407.8 and 419.9 nm, and with the solar spectrum in the Modtran 3.5 radiation model above 419.9 nm [*Anderson et al.*, 1993]. The ratio of the extraterrestrial irradiances was spectrally flat within ±3% in the wavelength range from 312 to 500 nm, and the average ratio was close to unity. This agreement is similar to the

one reported by *Bais* [1997] for Langley calibration of a Brewer spectroradiometer. The agreement between the different extraterrestrial spectra gives credibility to the accuracy of the absolute calibration of the direct irradiance.

The ozone values derived from the direct measurements have been checked against a colocated Brewer double–monochromator instrument, and differences were within ±1.5%. The absolute uncertainty in the aerosol optical depth is estimated to be within ±0.05. The spectral dependence of the aerosol optical depth was fitted using the Ångström formula and characterized by the two parameters α and β: $\tau_{\text{aerosol}} = \beta\lambda^{-\alpha}$, where λ is the wavelength in microns.

4. Radiative Transfer Model and Input Data

The radiative transfer model used is similar to the one used by *Mayer et al.* [1997] and *Kylling et al.* [1998]. It is based on the discrete ordinates radiative transfer (DISORT) algorithm developed by *Stamnes et al.* [1988]. This algorithm has been modified to account for the spherical shape of the atmosphere using the pseudospherical approximation [*Dahlback and Stamnes*, 1991]. The pseudospherical radiative transfer equation solver was operated in six–stream mode. Input data are the profile of ozone concentration; aerosol optical depth, single–scattering albedo, and phase function profiles; extraterrestrial spectrum; surface albedo; and time, and location of the measurement.

For the present analysis the sub–Arctic winter ozone profile from *Anderson et al.* [1986] was used. The ozone profile was scaled to the ozone column estimated from the direct irradiance spectra. The aerosol profile was taken from the spring–summer background aerosol profile of *Shettle* [1989]. The aerosol extinction depth at each wavelength was scaled using the Ångström α and β coefficients estimated from the direct irradiance spectra. The aerosol single–scattering albedo was set equal to 0.95 for all wavelengths. *Hansen* [1969] showed that the Henyey–Greenstein phase function can be used to replace more realistic Mie phase functions in multiple scattering approximations with no more than a few percent error in computed fluxes. Here the Henyey–Greenstein phase function was used with an asymmetry factor of 0.7. These are reasonable choices for typical aerosols in unpolluted regions [e.g., *Hansen and Travis*, 1974]. The sensitivity of the estimated surface albedo to these choices is discussed in section 5.

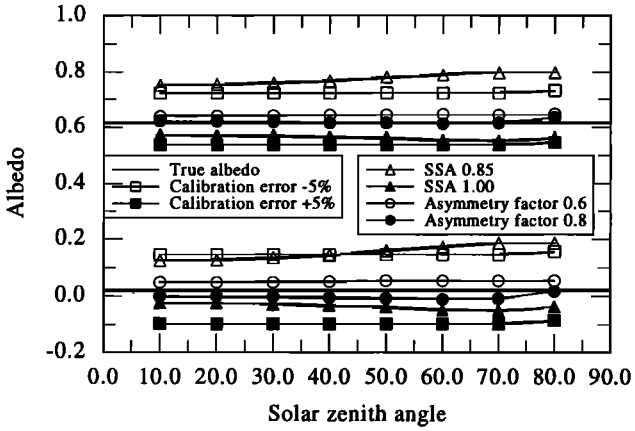

Figure 3. The simulated retrieved surface albedo at 350 nm as a function of the solar zenith angle. The upper solid line represents snow–covered ground, and the lower solid line represents lawn [*Feister and Grewe*, 1995]. The lines with open and solid squares show the retrieved albedo if the measured R (see equation (5)) is off by ±5%. Similar results are shown for variations in the aerosol asymmetry factor (lines with circles) and the aerosol single–scattering albedo (SSA; lines with triangles).

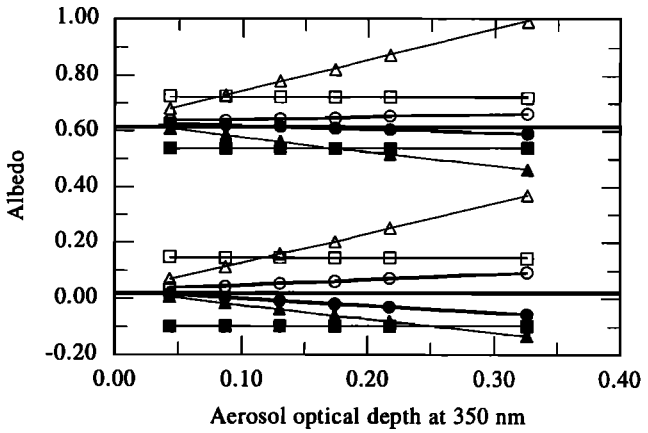

Figure 4. The simulated retrieved surface albedo at 350 nm and a solar zenith angle of 50.0 as a function of the aerosol optical depth at 350 nm, otherwise similar to Figure 3.

5. Sensitivity Analysis

The sensitivity of the retrieval method to measurement uncertainties and uncertainties in the model input data was checked by using model spectra. Spectra were simulated for two different surface albedos: snow–covered ground and lawn [*Feister and Grewe*, 1995]. Parameters that have an effect on the derived albedo were varied within reasonable limits for various solar zenith angles and aerosol optical depths. The error in the relative transmission between the direct and global measurements is about 5% (see section 3). In addition, the measured global irradiance is corrected for the non-ideal angular response of the input optics. The overall error in this correction procedure is ±4–5%. The combined uncertainty of these two errors is 7%. Increasing the ratio by 5% gives an underestimate (see equation (5)) of the derived albedo of about 0.1 (absolute value) at 350 nm (lines marked with solid squares, Figures 3 and 4). The underestimate is fairly constant with

solar zenith angle (Figure 3) and aerosol optical depth (Figure 4). Similarly, a decrease by 5% overestimates the derived albedo by a similar amount (lines marked with open squares in Figures 3 and 4). While the measurement–related error is relatively constant with solar zenith angle and aerosol optical depth for a single wavelength, it increases dramatically as a function of wavelength (Figure 5) owing to the lower sensitivity of the downwelling irradiance to the surface albedo as the wavelength increases (Figure 2).

To calculate the global transmittance needed in (5), assumptions had to be made about the aerosol single–scattering albedo and phase function. The sensitivity of the derived albedo to realistic variations in these parameters is also shown in Figures 3–5. Varying the asymmetry factor by ±0.1 from the base value of 0.70 affects the derived albedo by less than 0.02 except for large aerosol optical depths where the error may be up to 0.07 (Figure 4). Increasing the aerosol single–scattering albedo to 1.0 (conservative scattering) decreases the derived albedo owing to an overestimate of T_{global} in (5). The decrease is rather large, 0.16, for large aerosol optical depths (Figure 4). For aerosols that absorb more than the base calculations, single–scattering albedo of 0.85 versus 0.95 (base), the albedo is overestimated by up to 0.3. The sensitivity of the derived albedo to the choice of single–scattering albedo increases slightly with increasing solar zenith angle (Figure 3) and wavelength (Figure 5). It increases strongly with aerosol optical depth (Figure 4).

Generally, the sensitivity of the derived albedo to various parameters increases with wavelength (Figure 5) owing to the decrease in the Rayleigh scattering cross section (Figure 2). Of the parameters that have been discussed, the lack of knowledge of the aerosol single–scattering albedo and the measurement uncertainties are of most concern.

6. Results

Spectral measurements were performed from April to October 1997. The instrument was not operated during the months of July and August, and only limited data are available for September and October. The retrieval method only works for cloud–free situations. To select clear sky days or portions of days that were considered cloud–free, measurements made by a colocated Ground–based Ultraviolet Radiometer (GUV) multichannel narrow bandwidth filter instrument were inspected. The GUV instrument from Biospherical Instruments Inc., San Diego, similar to the one described by *Dahlback* [1996], records the irradiance in five narrow bands centered at 305, 313, 320, 340, and 380 nm with approximately 10 nm FWHM at 1 min intervals. After selecting the clear sky data all retrieved albedo spectra were visually examined, and clearly erroneous spectra were removed. Finally, only retrieved albedos for solar zenith angles smaller than 70° were kept except for the September data where slightly larger solar zenith angles were allowed. The final data set is summarized in Table 1. The variation of the derived albedo for a few selected wavelengths together with the snow depth measured at the nearby weather station is shown in Figure 6. The maximum snow depth in Tromsø in 1997 was a record 240 cm on April 29. On June 9 snow had vanished at the nearby local weather station, which is at approximately the same elevation as the site for the spectral measurements. However, in the surrounding mountains, snow was still present for approximately another month.

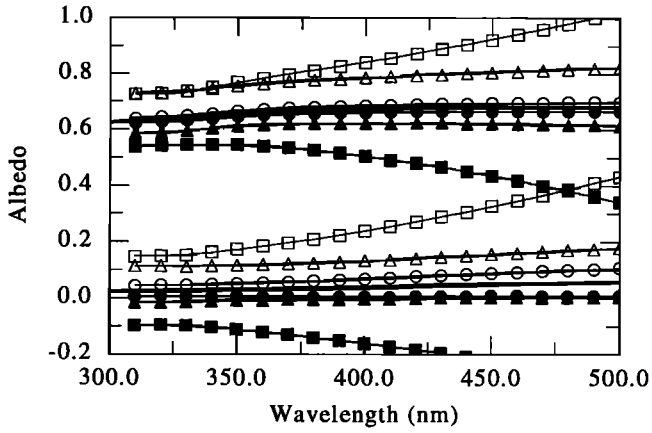

Figure 5. The simulated retrieved surface albedo for a solar zenith angle of 50.0 as a function of the wavelength. The aerosol optical depth at 350 nm was 0.16. Symbols are as those in Figure 3.

From Table 1 and Figure 6 we see that the snow depth increases between days 98 and 104. In the same period the surface albedo increases from 0.48 to 0.53 at 320 nm and from 0.55 to 0.71 at 450 nm. The snow depth decreases between days 104 and 105. The decrease in snow depth is associated with a decrease in the albedo similar in magnitude to the increase seen from days 98 to 104. This may be due to snow being blown or melted off roofs/trees, etc. The albedo reaches a maximum on day 120, just after the maximum snow depth is reached. The estimated albedo varies from 0.57 at 320 nm to 0.78 at 450 nm. Possibly, the albedo was slightly higher on day 119 when the snow depth had a maximum value of 240 cm. However, heavy snowfall made measurements impossible during that day. After day 120 the snow depth decreases as does the albedo, see, for example, days 128 and 129. The albedo on day 150 is lower than that on day 129. However, the downward trend in the albedo seen from days 120 to 129 is interrupted. The snow decreased from 179 to 66 cm between days 129 and 150. However, the code used to describe the snow conditions at the local weather station states that the ground was still completely covered by snow on day 150. Only snow on the trees, some house roofs, and the main roads would have been gone. From day 150 the albedo decreases until day 161. For

Table 1. The Derived Albedo and Minimum and Maximum Values of Some Atmospheric Parameters

Date	Day Number	Ozone, DU	τ at 350 nm	Solar Zenith Angle, deg	Spectra Number	Albedo, nm 320	350	400	450	Snow Depth, cm
April 8	98	262.3–271.5	0.120–0.148	62.4–68.9	15	0.48	0.52	0.53	0.55	190
April 14	104	319.7–330.8	0.065–0.079	60.2–65.4	8	0.53	0.61	0.65	0.71	197
April 15	105	320.4–332.4	0.106–0.151	59.8–65.7	14	0.50	0.57	0.58	0.60	193
April 23	113	256.6–310.9	0.188–0.236	59.5–64.9	3	0.49	0.66	0.72	0.78	213
April 30	120	255.8–297.4	0.148–0.350	54.8–58.7	8	0.57	0.68	0.73	0.78	233
May 8	128	297.8–311.7	0.135–0.213	52.5–62.6	24	0.49	0.59	0.61	0.64	188
May 9	129	306.6–321.7	0.229–0.305	52.2–63.8	17	0.46	0.57	0.60	0.63	179
May 30	150	335.1–341.0	0.122–0.164	47.9–61.2	9	0.45	0.54	0.59	0.66	66
June 8	159	263.8–295.9	0.383–0.574	47.2–57.8	5	0.31	0.45	0.54	0.56	3
June 10	161	293.1–303.4	0.262–0.348	46.6–54.5	8	0.27	0.39	0.43	0.44	0
June 12	163	293.3–305.1	0.315–0.374	46.5–49.0	8	0.21	0.35	0.40	0.45	0
June 14	165	284.8–297.1	0.377–0.531	46.7–55.8	9	0.20	0.37	0.44	0.49	0
June 15	166	288.9–303.5	0.337–0.426	46.4–60.9	19	0.25	0.39	0.50	0.56	0
June 16	167	301.3–320.1	0.215–0.273	46.3–61.7	21	0.14	0.29	0.38	0.44	0
June 17	168	290.7–329.2	0.191–0.284	46.5–69.5	22	0.10	0.25	0.33	0.38	0
June 23	174	332.8–341.5	0.194–0.281	46.3–61.8	9	0.19	0.33	0.41	0.46	0
Sept. 9	252	262.7–273.5	0.091–0.153	64.8–72.4	3	0.08	0.18	0.17	0.16	0

DU, Dobson unit.

day 154 the weather station reports that more than half the ground was still snow covered, while for day 156, less than half of the ground was covered by snow. Hence the rapid decrease in albedo after day 150. Only patches of snow were left at the nearby site of the local weather station after day 159. They were gone on day 164. However, the nearby mountains were snow covered for approximately yet another month. After day 161 the derived albedo appears to be somewhat noisy, especially for the longer wavelengths. The aerosol optical depth is comparatively much larger for days 159 to 166 ranging from 0.262 to 0.574. For comparison, the Rayleigh optical depth at 350 nm is 0.626. Hence the estimated albedo for days within this period is more vulnerable to the assumptions made about the aerosol single-scattering albedo (Figure 4). However, for day 174 the aerosol is not particularly large; nevertheless, the albedo makes a jump. The reason for this increase is not clear. We note, however, that the instrument is operated during severe weather conditions that may affect the direct and global entrance optics differently. This might affect the measured direct/global irradiance

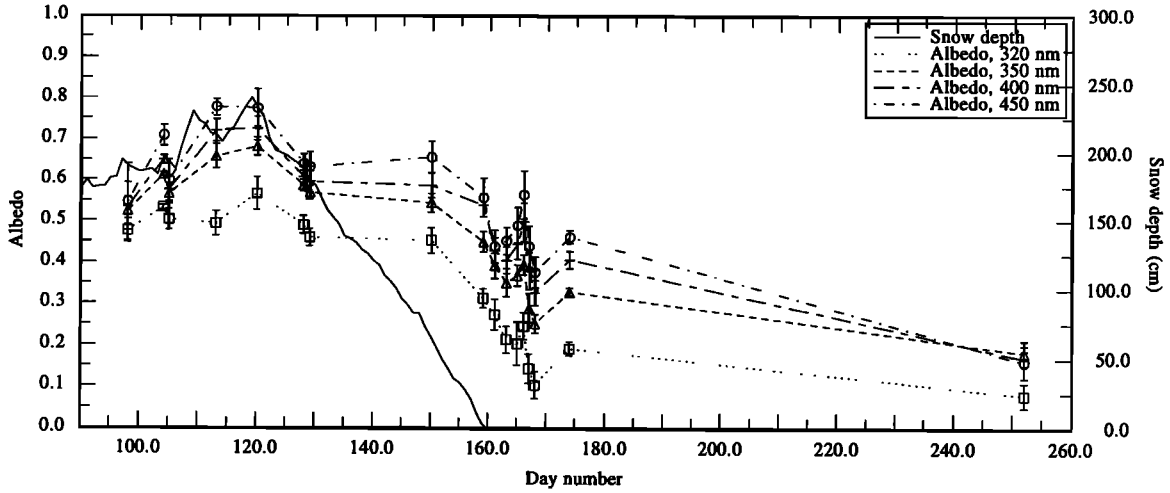

Figure 6. The effective spectral surface albedo (left axis) for four wavelengths as a function of day number in 1997 for Tromsø, Norway. The albedo results shown are daily averages of albedos derived under cloud-free conditions. The error bars denote the standard deviation of the variability in the albedo measurements of a particular day. The snow depth (solid line, right axis) measured at the local weather station is also shown.

ratio and hence the derived albedo. For the days 120, 128, and 129 the decrease in the albedo follows the decrease in the snow depth. While the rate of decrease in the surface albedo is similar for days 150 to 168, the decrease in the albedo is delayed compared with the decrease in the snow depth. It is not possible to estimate the date for the onset of this delay owing to the lack of data. The delay may, however, reflect the increasing importance of the contributions from the surrounding mountains. In September all snow in the surrounding mountains is gone, and the albedo is at its lowest.

Wavelength dependencies of the derived albedo for a few selected days are shown in Figure 7. Generally, the albedo increases with wavelength for all days except for September 9. However, for wavelengths larger than 480 nm a decrease is seen for most days. This decrease is not believed to be real but rather due to uncertainties in the retrieval technique. Also, the wavelength dependence in the September data is believed to have the same cause. The wavelength dependence is somewhat stronger in the data presented here than it is in those reported by *Feister and Grewe* [1995].

The surface around the measurement site is highly inhomogeneous, and the surfaces are most likely not Lambertian reflecting surfaces. Hence solar azimuth dependent effects may be present in the measured data. The sensitivity of the method to azimuth dependent effects is believed to be rather small for wavelengths below approximately 400 nm where the diffuse radiation makes a considerable contribution to the global irradiance for the solar zenith angles encountered during this study (Figure 2). Note that in the calculations presented in Figure 2, aerosols are not included. Hence the lines represent upper limits for the direct/global ratio. Above 400 nm the direct irradiance becomes increasingly dominant and azimuth effects may be present. The magnitude of the azimuth effect is difficult to assess because of the lack of detailed information of the types of surfaces surrounding the observation site at a given time. For a few days, spectra were available for the whole day. These diurnal variations were carefully examined for azimuth effects; however, it is difficult to say with confidence that azimuth effects are present in the estimated surface albedo. However, the absence of azimuth effects can not be ruled out either.

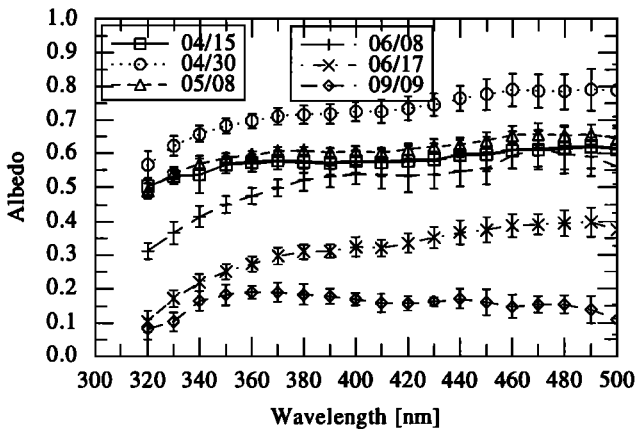

Figure 7. The wavelength dependence of the regional spectral surface albedo for a few selected days in Tromsø in 1997. Results averaged over the clear sky portions of the day are shown together with the standard deviation of all data points of that day (error bars).

7. Effect of the Ocean

The derived albedo values are considerably lower than those for a homogeneous snow–covered surface [*Warren and Wiscombe*, 1980; *Wiscombe and Warren*, 1980]. To investigate the effect of the surrounding ocean on the irradiance measurements, a three-dimensional Monte Carlo (MC) model was developed. The MC model, which is an improved version of the model used by *Mayer et al.* [1998], traces a multitude of photons on their individual random paths through the atmosphere. Rayleigh scattering, aerosol scattering and absorption, ozone absorption, and reflection by a Lambertian surface are included in the model. The atmosphere, which was assumed to be homogeneous in the horizontal directions, was divided into 36 vertical layers between 0 and 50 km. The midlatitude-summer profiles of air pressure, temperature, and ozone concentration were taken from *Anderson et al.* [1986]. The inhomogeneous surface albedo was parameterized by sampling the map shown in Figure 1 in area elements of 2×2 km^2, where each element was assigned either the albedo of land or water. The albedo of the sea was set to 0.07, while the albedo of the land was set to 0.95 and 0.8, which corresponds to fresh and aged snow, respectively. The model considered the whole region shown in Figure 1, 200×200 km^2. For some case studies, topography was also included into the MC model. For this purpose, data from the GTOPO30 data set (Global 30 Arc Second Elevation data set, available at http://-edcwww.cr.usgs.gov/landdaac/gtopo30/gtopo30.html) were regridded to 1×1 km^2 resolution using the Generic Mapping Tools (GMT) [*Wessel and Smith*, 1991, 1995]. Between these data points, the surface was interpolated bilinearely to calculate the appropriate surface elevation and inclination at any location. Whenever topography was included for an investigation, it will be noted explicitly in the text. Although some of the mountains surrounding Tromsø are higher than 1000 m asl, they have no direct shading effect on the measurement site for the solar zenith angles considered.

Calculations were performed for atmospheric conditions representative for those found in Tromsø in 1997. The total ozone column was set to 340 Dobson units (DU), the aerosol extinction optical depth at 350 nm was 0.2, and the aerosol single-scattering albedo and asymmetry factor were set to 0.95 and 0.7, respectively. The results of the MC model for a homogeneous surface albedo showed an agreement of better than 1% with the discrete ordinate model DISORT of *Stamnes et al.*

[1988], which has also been used for the plane-parallel calculations in sections 5 and 6. More details of the MC model will be published elsewhere.

Figure 8 shows the most important parameters determining the area that affects the local irradiance. In Figure 8a the fraction, $\bar{s}$, of the upwelling radiation which is reflected downward by the atmosphere is shown. This atmospheric reflectivity increases toward shorter wavelengths owing to the increase in the Rayleigh scattering optical depth. Below 320 nm, however, absorption by ozone becomes important, decreasing the reflectivity in the UV–B range. The second important parameter determining the effective area is shown in Figure 8b: the average horizontal distance a photon, which is reflected at the surface, travels before it hits the surface again. Because of the increasing Rayleigh scattering optical depth, this distance decreases toward shorter wavelengths. Note that for a Lambertian surface, none of the parameters depend on the solar zenith angle, because all information about the direction of incidence is lost after the first reflection at the surface. The effective area affecting the local irradiance is determined by a combination of both parameters.

The MC model was used to calculate the irradiance at Tromsø for winter conditions, where the land was assumed to be completely snow covered with an albedo of 0.8 (aged snow) and 0.95 (fresh snow), while the sea was completely snow free with an albedo of 0.07. The calculated values of the irradiance were then used to determine the "effective albedo" at the measurement site in Tromsø. This effective albedo is shown in Figure 9. The absolute values clearly indicate that the irradiance at the site is influenced by both surfaces, because the effective albedo is considerably smaller compared to

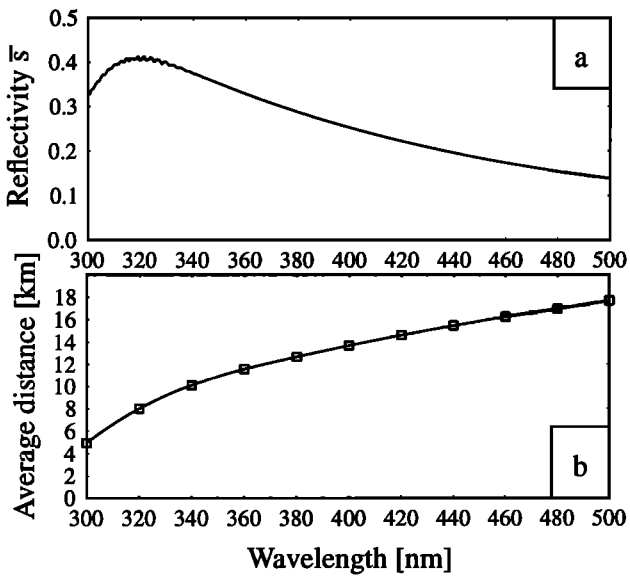

Figure 8. (a) Downward reflectivity $\bar{s}$ of the atmosphere. (b) The average horizontal distance a photon, which is reflected at the surface, travels before it hits the surface again.

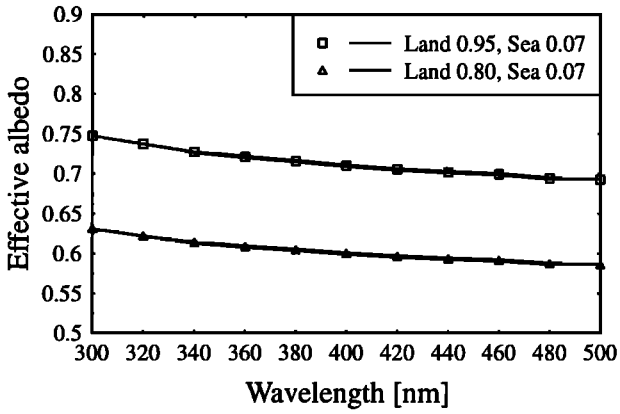

Figure 9. Effective albedo for Tromsø as a function of wavelength.

the value corresponding to snow. The decrease of the effective albedo with wavelength can be explained by the increase of the averaged horizontal displacement of a photon shown in Figure 8b: With increasing wavelengths, the irradiance is more and more affected by the open sea, which is about 25 km away. Thus, even with a surface albedo which is assumed to be independent of wavelength, a wavelength dependence is introduced into the effective albedo. The measured albedo, in contrast to the MC results, showed an increase with wavelength. The discrepancies between model and measurements, however, are within the uncertainties of the experimentally derived effective albedo. We note that the albedo values used over land assume that the surface is completely covered by snow. On the island of Tromsø and the surrounding mainland and islands this is never true since trees, houses, rocks, etc. penetrate through the snow and lower the local albedo. The MC calculations thus represent upper limits. Furthermore, a small wavelength dependence in the albedo of snow, for example, as measured by *Feister and Grewe* [1995], may attribute to the discrepancies. Finally, topography has an influence on the surface irradiance which is implicitly included in the derived effective albedo. Using the Monte Carlo model including topography to calculate the irradiance in a case study for 50° solar zenith angle and noontime (sun in the south), we found that the effect of topography on surface irradiance as well as on the ratio of direct to global irradiance in Tromsø is less than 1% for the wavelength range under consideration. Although the effect on irradiance is very small, the change of the derived albedo in the visible range of the spectrum might be significantly higher (see Figure 5). A quantitative investigation of the influence of topography on the derived albedo, however, is far beyond the scope of this paper. It would require computationally intensive Monte Carlo calculations for a variety of solar zenith and azimuth angles and atmospheric compositions because these parameters definitely determine the magnitude of the effect.

Herman and Celarier [1997] reported monthly averaged surface reflectivites based on Nimbus 7/Total Ozone Mapping Spectrometer (TOMS) data from the years 1978–1993. The resolution of the TOMS data is $1.25° \times 1°$, which is approximately 50×110 km^2 at the latitude of Tromsø. For the pixel covering Tromsø the values at 380 nm for the months of April, May, June, and September are 0.36, 0.15, 0.08, and 0.06, respectively. This is somewhat smaller than the values reported here (Table 1). The pixel east of Tromsø has the values 0.57, 0.25, 0.10, and 0.05 for the same months, which is closer to the values reported here. It is noted that the TOMS data represent an average over 14.5 years of data where pixels with the lowest reflectivity were selected to avoid as best as possible any potential cloud problems. As such, the TOMS surface reflectivities are not directly comparable with the albedo values presented here. Furthermore, the TOMS data set represents a small subset of possible solar zenith angle and viewing angle combinations. However, considering the differences in spatial and temporal scale and the very different methodologies, the two different albedo data sets agree reasonably well.

8. Discussion and Conclusions

A method has been developed to retrieve an effective regional spectral surface albedo from direct and global UV and visible irradiance measurements. The sensitivity of the method to various atmospheric parameters; uncertainties in aerosol single–scattering albedo and asymmetry factor; and instrumental parameters, calibration, and cosine response errors has been investigated. The method is most sensitive to measurement uncertainties related to the calibration of the instrument and the procedure used to correct for the nonideal angular response of the detector. At high aerosol optical depths the method is sensitive to the uncertainties in the aerosol single-scattering albedo.

The method has been used to analyze data measured in 1997 in Tromsø, Norway. The derived albedo obtained a maximum of 0.57 and 0.78 at 320 and 450 nm, respectively, when the snow depth was at maximum. The corresponding values for snow–free conditions, that is, when the snow is also gone in the surrounding mountains, were 0.08 and 0.16. The absolute uncertainty in these values is estimated to be 0.1 for the short wavelengths and to increase to 0.2 for the longer wavelengths. The implication of these uncertainties definitely depends on the application: For example, reversing the argument from Figure 5, an uncertainty of 0.2 in the surface albedo at 500 nm would lead to an uncertainty of less than 5% when used to calculate spectral irradiance.

A three–dimensional Monte Carlo model has been used to calculate the effective albedo at Tromsø, assuming that the land was completely covered with the snow while the sea was completely snow free. The surrounding ocean was found to decrease the effective albedo by approximately 0.2 compared to a completely snow–covered surface. The decrease was found to be wavelength dependent because with increasing wavelength the local irradiance is more and more influenced by the open sea. However, the MC results and the measured albedo showed different wavelength dependencies, with the MC results decreasing with increasing wavelength and the measurements increasing. While the differences are within the uncertainties of the measurements, further investigations are required both to improve the albedo retrieval method and to understand the three–dimensional effects on the radiation field.

To improve the quality of the retrieved albedo, a better characterization of the aerosol would be useful together with improved calibration accuracy. Furthermore, an unambiguous method to clearly identify noncloudy situations might improve the quality of this type of data sets.

At high latitudes, such as at Tromsø, snow may be on the ground until early summer, hence increasing the UV radiation levels considerably. The presented method may allow us to improve our understanding of the coupling between snow cover, surface albedo, and UV radiation levels. The libRadtran radiative transfer model used for the retrieval calculations is available by anonymous ftp to ftp.geofysikk.uio.no, cd pub/outgoing/arveky.

Appendix: Alternative Derivation of Equation (5)

The downward surface irradiance in a planetary atmosphere consists of three parts [*Chandrasekhar*, 1960, p. 272–273]: the reduced direct irradiance,

$$\pi \mu_0 E_\odot e^{-ch(\tau_1,\mu_0)}, \tag{A1}$$

the diffusely transmitted irradiance,

$$\begin{aligned}\int_0^1 \int_0^{2\pi} \frac{E_\odot}{4\mu}\, T(\mu,\phi;\mu_0,\phi_0)\mu d\mu d\phi_0 &= \pi E_\odot \frac{1}{2}\int_0^1 T^{(0)}(\mu;\mu_0)d\mu \\ &= \pi E_\odot t(\mu_0),\end{aligned} \tag{A2}$$

and the flux due to radiation reflected upward by the surface and scattered back to the surface by the atmosphere,

$$\begin{aligned}\int_0^1 \int_0^{2\pi} I_g^{(\mathrm{ref})}(-\mu)\mu d\mu d\phi &= 2\pi I_g \int_0^1 s(\mu)d\mu \\ &= \pi I_g \bar{s}.\end{aligned} \tag{A3}$$

Here τ_1 is the total optical depth of the atmosphere, μ_0 is the cosine of the solar zenith angle, $E_\odot$ is the extraterrestrial solar flux, $ch(\tau_1,\mu_0)$ is the Chapman function [*Dahlback and Stamnes*, 1991], $T(\mu,\phi;\mu_0,\phi_0)$ is the transmission function, $T^{(0)}(\mu;\mu_0)$ is the azimuthally av-

eraged transmission function, and $t(\mu_0)$ is the transmissivity [*Stamnes*, 1982]. Furthermore, I_g is the outward radiance from the Lambertian surface, and $I_g^{(\mathrm{ref})}(-\mu)$ is the part of I_g reflected by the atmosphere. The angular averaged reflectivity of the atmosphere, $\overline{s}$, is defined by

$$\begin{aligned}\overline{s} &= 2\int_0^1 s(\mu)d\mu \\ &= \frac{1}{2\pi}\int_0^1\int_0^1\int_0^{2\pi} S(\mu,\phi;\mu_0,\phi_0)d\phi_0 d\mu d\mu_0 \quad \text{(A4)}\end{aligned}$$

where $S(\mu,\phi;\mu_0,\phi_0)$ is the scattering function. We note that $\overline{s}$ is calculated with isotropic illumination from below.

Combining (A1)–(A3), the global downward irradiance becomes

$$E^{\downarrow}(\tau_1) = \pi[\mu_0 E_{\odot}\gamma_1(\mu_0) + I_g\overline{s}], \quad \text{(A5)}$$

where

$$\gamma_1(\mu) = e^{-ch(\tau_1,\mu)} + \frac{t(\mu)}{\mu}. \quad \text{(A6)}$$

The outward flux must equal the reflected incoming flux:

$$\pi I_g = \Lambda E^{\downarrow}(\tau_1). \quad \text{(A7)}$$

Substituting (A7) into (A5), the outward radiance becomes

$$I_g = \frac{\Lambda}{1-\overline{s}\Lambda}\mu_0 E_{\odot}\gamma_1(\mu_0). \quad \text{(A8)}$$

The global downward irradiance, equation (A5), may thus be written as

$$E^{\downarrow}(\tau_1) = \pi\mu_0 E_{\odot}\gamma_1(\mu_0)\left[1 + \frac{\overline{s}\Lambda}{1-\overline{s}\Lambda}\right]. \quad \text{(A9)}$$

The second term within the parentheses is the contribution to the surface irradiance by radiation reflected from the surface and scattered downward again by the atmosphere.

Dividing the reduced direct irradiance (equation (A1)) by the global downward irradiance (equation (A9)), equating the result with R derived from measurements and solving for Λ gives (5).

Acknowledgments. We would like to thank Lars Næsheim for providing the snow depth data. This work was done within the framework of the UVRAPPF project funded by the European Commission (contract ENV4-CT95-0165). A.K. also acknowledges support from the Norwegian Research Council. B.M. was supported by a research grant by the German Academic Exchange Service (DAAD).

References

Anderson, G., S. Clough, F. Kneizys, J. Chetwynd, and E. Shettle, AFGL atmospheric constituent profiles (0-120 km), *Tech. Rep. AFGL-TR-86-0110*, Air Force Geophys. Lab., Hanscom Air Force Base, Bedford, Mass., 1986.

Anderson, G. P., et al., MODTRAN2: Suitability for remote sensing, in *Atmospheric Propagation and Remote Sensing, SPIE Conf. Ser.*, vol. 1968, edited by A. Kohnle and W. B. Miller, pp. 514–525, Soc. of Photo–Optical–Instrum. Eng., Bellingham, Wash., 1993.

Bais, A. F., Absolute spectral measurements of direct solar ultraviolet irradiance with a Brewer spectrophotometer, *Appl. Opt.*, *36*, 5199–5204, 1997.

Blumthaler, M., and W. Ambach, Solar UVB–albedo of various surfaces, *Photochem. Photobiol.*, *48*, 85–88, 1988.

Chandrasekhar, S., *Radiative Transfer*, Dover, Mineola, N. Y., 1960.

Dahlback, A., Measurements of biologically effective UV doses, total ozone abundances, and cloud effects with multichannel, moderate bandwidth filter instruments, *Appl. Opt.*, *35*, 6514–6521, 1996.

Dahlback, A., and K. Stamnes, A new spherical model for computing the radiation field available for photolysis and heating at twilight, *Planet. Space Sci.*, *39*, 671–683, 1991.

Degünther, M., R. Meerkötter, A. Albold, and G. Seckmeyer, Case study on the influence of inhomogeneous surface albedo on UV irradiance, *Geophys. Res. Lett.*, *25*, 3587–3590, 1998.

Feister, U., and R. Grewe, Spectral albedo measurements in the UV and visible region over different types of surfaces, *Photochem. Photobiol.*, *62*, 736–744, 1995.

Hansen, J. E., Exact and approximate solutions for multiple scattering by cloudy and hazy planetary atmospheres, *J. Atmos. Sci.*, *26*, 478–487, 1969.

Hansen, J. E., and L. D. Travis, Light scattering in planetary atmospheres, *Space Sci. Rev.*, *16*, 527–610, 1974.

Herman, J. R., and E. A. Celarier, Earth surface reflectivity climatology at 340–380 nm from TOMS data, *J. Geophys. Res.*, *102*, 28,003–28,011, 1997.

King, M. D., Determination of the ground albedo and the index of absorption of atmospheric particulates by remote sensing, II, Application, *J. Atmos. Sci.*, *36*, 1072–1083, 1979.

King, M. D., and B. M. Herman, Determination of the ground albedo and the index of absorption of atmospheric particulates by remote sensing, I, Theory, *J. Atmos. Sci.*, *36*, 163–173, 1979.

Kylling, A., A. F. Bais, M. Blumthaler, J. Schreder, C. S. Zerefos, and E. Kosmidis, The effect of aerosols on solar UV irradiances during the Photochemical Activity and Solar Ultraviolet Radiation campaign, *J. Geophys. Res.*, *103*, 26,051–26,060, 1998.

Lenoble, J., Modeling of the influence of snow reflectance on ultraviolet irradiance for cloudless sky, *Appl. Opt.*, *37*, 2441–2447, 1998.

Mayer, B., G. Seckmeyer, and A. Kylling, Systematic long–term comparison of spectral UV measurements and UVSPEC modeling results, *J. Geophys. Res.*, *102*, 8755–8767, 1997.

Mayer, B., A. Kylling, S. Madronich, and G. Seckmeyer, Enhanced absorption of UV radiation due to multiple scattering in clouds: Experimental evidence and theoretical explanation, *J. Geophys. Res.*, *103*, 31,241–31,254, 1998.

McKenzie, R. L., M. Kotkamp, and W. Ireland, Upwelling UV spectral irradiances and surface albedo measurements at Lauder, New Zealand, *Geophys. Res. Lett.*, *23*, 1757–1760, 1996.

Ricchiazzi, P., and C. Gautier, Investigation of the effect of surface heterogeneity and topography on the radiation environment of Palmer Station, Antarctica, with a hybrid 3–D radiative transfer model, *J. Geophys. Res.*, *103*, 6161–6176, 1998.

Ricchiazzi, P., C. Gautier, and D. Lubin, Cloud scattering optical depth and local surface albedo in the Antarctic:

Simultaneous retrieval using ground-based radiometry, *J. Geophys. Res.*, *100*, 21,091–21,104, 1995.

Shettle, E. P., Models of aerosols, clouds and precipitation for atmospheric propagation studies, paper presented at Conference on Atmospheric Propagation in the UV, Visible, IR and MM-Region and Related System Aspects, NATO Adv. Group for Aerosp. Res. and Dev., Copenhagen, 1989.

Stamnes, K., Reflection and transmission by a vertically inhomogeneous planetary atmosphere, *Planet. Space Sci.*, *30*, 727–732, 1982.

Stamnes, K., S.-C. Tsay, W. Wiscombe, and K. Jayaweera, Numerically stable algorithm for discrete-ordinate-method radiative transfer in multiple scattering and emitting layered media, *Appl. Opt.*, *27*, 2502–2509, 1988.

Warren, S. G., and W. J. Wiscombe, A model for the spectral albedo of snow, II, Snow containing atmospheric aerosols, *J. Atmos. Sci.*, *37*, 2734–2745, 1980.

Wessel, P., and W. H. F. Smith, Free software helps map and display data, *Eos Trans. AGU*, *72-(41)*, 441, 1991.

Wessel, P., and W. H. F. Smith, New version of the Generic Mapping Tools released, *EOS Trans. AGU*, *76-(33)*, 329, 1995.

Wiscombe, W. J., and S. G. Warren, A model for the spectral albedo of snow, I, Pure snow, *J. Atmos. Sci.*, *37*, 2712–2733, 1980.

Woods, T. N., et al., Validation of the UARS solar ultraviolet irradiances: Comparison with the Atlas 1 and 2 measurements, *J. Geophys. Res.*, *101*, 9541–9569, 1996.

A. Kylling, NILU–Kjeller, N-2027 Kjeller, Norway. (arve.kylling@nilu.no)

B. Mayer, National Center for Atmospheric Research, P.O. Box 3000, Boulder, CO 80307, (bmayer@ucar.edu)

T. Persen, Kværner Engineering, 4000 Stavanger, Norway. (tore.persen@aop.akermar.com)

T. Svenøe, NILU–Tromsø, N-9005 Tromsø, Norway. (trond.svenoe@nilu.no)

(Received November 5, 1998; revised March 23, 1999; accepted April 20, 1999.)